Substituent Effects in the Binding of Alkali Metal Ions to Pyridines, Studied by Threshold Collision-Induced Dissociation and ab Initio Theory: The Methylpyridines†

M. T. Rodgers

Department of Chemistry, Wayne State University, Detroit, Michigan 48202

Received: November 3, 2000; In Final Form: December 12, 2000

Threshold collision-induced dissociation of M^+(*x*-methylpyridine) with xenon is studied using a newly constructed guided ion beam mass spectrometer, described in detail here. M^+ include the following alkali metal ions: Li^+, Na^+, and K^+. All three structural isomers are examined, x = ortho, meta, and para. In all cases, the primary product corresponds to endothermic loss of the intact *x*-methylpyridine molecule, with minor production of MXe^+ formed by ligand exchange. The cross section thresholds are interpreted to yield zero and 298 K bond dissociation energies for M^+−*x*-methylpyridine after accounting for the effects of multiple ion−molecule collisions, internal energy of the reactant ions, and dissociation lifetimes. Ab initio calculations at the MP2(full)/6-31G* level of theory are used to determine the structures of these complexes and provide molecular constants necessary for the thermodynamic analysis of the experimental data. Theoretical bond dissociation energies are determined from single point calculations at the MP2(full)/6-311+G(2d,2p) level using the MP2(full)/6-31G* geometries. Excellent agreement between theory and experiment is found for the Na^+ and K^+ systems, whereas the theoretical BDEs to Li^+ systems are systematically low but still within experimental error. Good agreement is found for the single previously measured bond dissociation energy of Li^+ to *m*-methylpyridine.

Introduction

In recent work, we have developed methods to allow the application of quantitative threshold collision-induced dissociation methods to obtain accurate thermodynamic information on increasingly large systems.[1−10] One of the driving forces behind these developments is our interest in applying such techniques to systems having biological relevance. In addition, we seek to perform accurate thermochemical measurements that provide absolute anchors for metal cation affinity scales over an ever-broadening range of energies and systems.

Among the systems examined in these earlier studies are a number of nitrogen-based heterocycles and several of the nucleic acid bases with alkali, alkaline earth, and transition metal ions.[5−10] These systems were chosen as models of nocovalent interactions with nucleic acids and a wide variety of nitrogen-based heterocycles of biological importance. We began these investigations with ligands possessing only a single functional group. This fundamental approach has allowed us to systematically examine the influence of the electronic structure of the metal ion, the polarizability, the dipole moment, and the tautomeric form of the ligand, as well as the effects that chelation and steric interactions have upon the strength of binding in these systems. Because the nucleic acid bases, modified bases, and other biologically relevant systems possess amino, hydroxy, and methyl substituents, we have recently initiated studies to extend this work by studying substituted pyridine systems. These theoretical and experimental studies examine the intrinsic effects of varying the chemical identity of both the metal ion and the substituent (CH_3, NH_2, and OH) as well as the position of the substituent relative to the nitrogen atom-binding site (ortho, meta, and para).

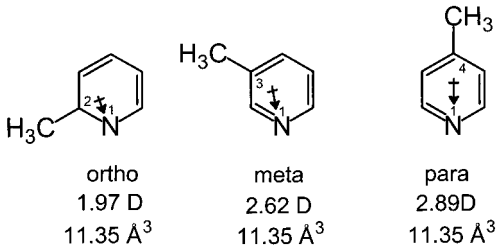

Figure 1. Structure of the *x*-methylpyridine molecules. Properly scaled dipole moment in Debye are shown for each as an arrow. Values for the dipole moment are determined from theoretical calculations performed here. The estimated polarizability is also shown (ref 11).

In the present study, we use guided ion beam mass spectrometry to collisionally excite complexes of M^+ bound to the structural isomers (ortho, meta, and para) of *x*-methylpyridine (*x*-MePyr), where $M^+ = Li^+$, Na^+, and K^+. The structures of the *x*-MePyr isomers are shown in Figure 1 along with their calculated dipole moments (determined here) and estimated polarizabilities.[11] The kinetic energy-dependent cross sections for the collision-induced dissociation (CID) processes are analyzed using methods developed previously.[3] The analysis explicitly includes the effects of the internal and translational energy distributions of the reactants, multiple collisions, and the lifetime for dissociation. We derive M^+−*x*-MePyr bond dissociation energies (BDEs) for all of the complexes, and compare these results to ab initio calculations performed here. Comparison is also made in the single case, Li^+(*m*-MePyr), where a literature value is available.[12−14]

† Part of the special issue "Aron Kuppermann Festschrift". In honor of Aron Kuppermann on the occasion of his 75th birthday and in thanks for his many contributions to both experimental and the theoretical studies of chemical reaction dynamics.

10.1021/jp004055z CCC: $20.00
Published on Web 02/14/2001

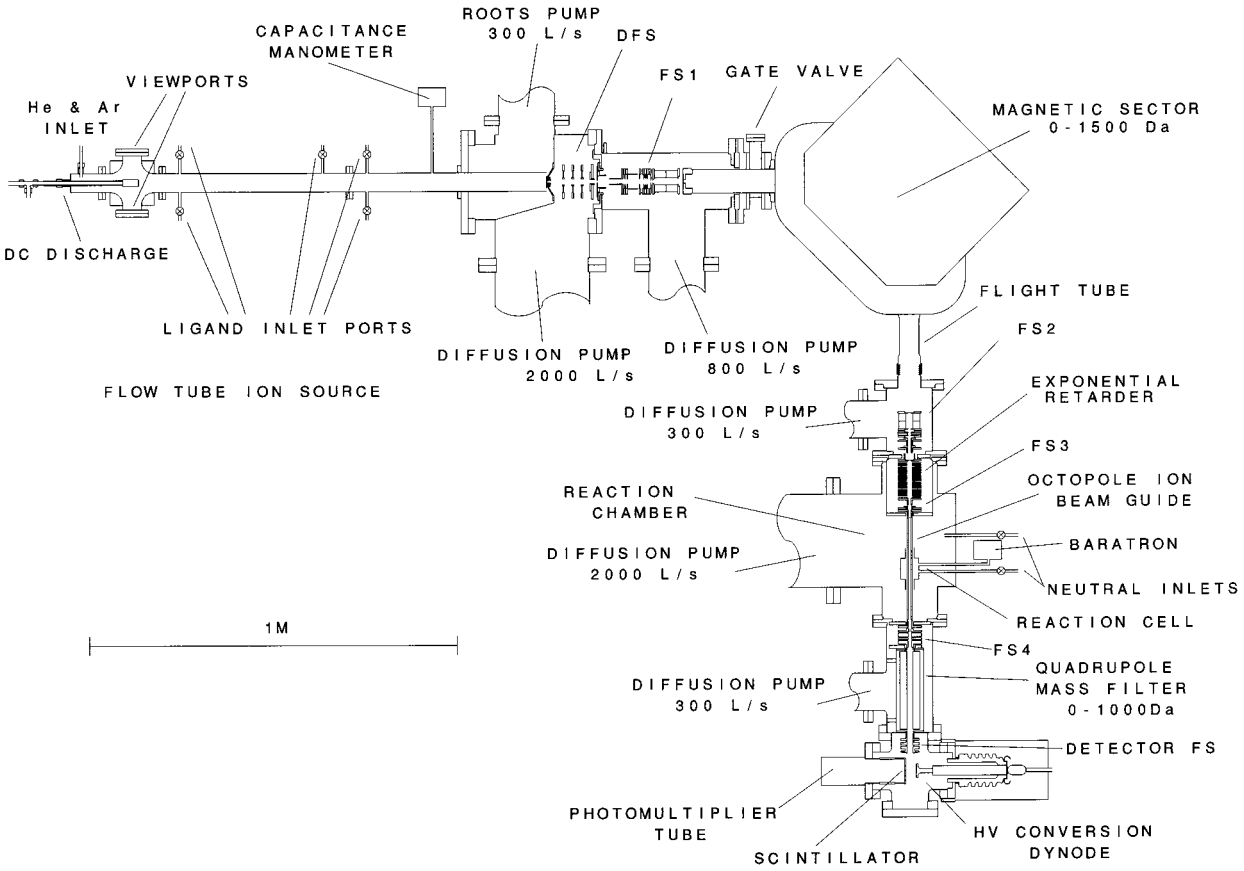

Figure 2. Schematic diagram of the guided ion beam tandem mass spectrometer.

Experimental Section

Instrument Overview. A schematic of the guided ion beam tandem mass spectrometer recently constructed in our laboratories is shown in Figure 2. The vacuum system comprises six regions that are individually pumped: (1) the flow tube ion source, (2) the first differentially pumped chamber, (3) the second differentially pumped region, (4) the magnetic sector flight tube and third differentially pumped chamber, (5) the reaction chamber, and (6) the detector chamber. All regions are pumped by diffusion pumps with integral water baffles except for the flow tube ion source, which is pumped by a roots blower. Base pressure in the apparatus is in the low 10^{-8} Torr region, whereas during operation, the pressure rises differently in different parts of the apparatus. Details of these various regions are provided in the following sections.

Flow Tube Ion Source. Ions are generated in a flow tube ion source.[15−17] The stainless steel flow tube has an inner diameter of 4.7 cm and is 1.0 m long. It is made of three separate sections allowing the length to be varied between 0.2 and 1.0 m depending upon the sections used. We routinely use the full length to provide maximal thermalizing collisions with the buffer gases. However, shorter lengths can be used to increase the intensity of ions by minimizing losses due to radial diffusion toward the walls along the length of the tube. Helium is used as the buffer gas at a flow rate of 4000 to 6000 sccm, resulting in a stagnation pressure of 0.5 to 1.0 Torr. The flow is maintained by a roots blower and mechanical pump (Edwards model EH1200/E2 M175) with a combined pumping speed of approximately 258 L s^{-1} over the range of typical operating pressures we employ.

In the present work, metal ions are generated in a continuous dc discharge by argon ion sputtering of a cathode, made from tantalum or iron, with a cavity containing the alkali metal. Typical operating conditions of the discharge are 1.5−3.5 kV and 15−30 mA in a flow of roughly 10% argon in helium for the experiments performed here. The M^+(*x*-MePyr) complexes are formed by associative reactions of the metal ion with the neutral *x*-MePyr, which is introduced into the flow 50 cm downstream from the dc discharge. The flow conditions used in this ion source provide in excess of 10^4 collisions between an ion and the buffer gas, which should thermalize the ions both vibrationally and rotationally. In our analysis of the data, we assume that the ions produced in this source are in their ground electronic states and that the internal energy of the M^+(*x*-MePyr) complexes is well described by a Maxwell−Boltzmann distribution of ro-vibrational states at 298 K. Previous work has shown that these assumptions are generally valid.[18−23]

Differential Focusing Stage. Ions are effusively sampled from the flow tube through a 1.0 mm aperture in a nose cone plate (molybdenum coated with colloidal graphite) and are gently focused by a series of aperture lenses in the differential focusing stage (DFS). Lens voltages in this region are typically kept below about 25 V in order to avoid energetic collisions that might internally excite the ions. As nearly all of these collisions are with the He flow gas, the center-of-mass energy available in such collisions is quite small. The DFS lenses have an open design to maximize gas conductance, which reduces the probability of energetic collisions in this region. The pressure in the differential region is maintained at 2×10^{-6} Torr (uncorrected for ion gauge sensitivity to helium) during operation of the flow tube by a 2000 L s^{-1} diffusion pump with water cooled baffles (Edwards Diffstak Mk2 250/2000P). At this pressure, the probability of a collision in this differential region (assuming a cross section of 25 $Å^2$) is only 0.2%. Differential

pumping is maintained from the following region by a 5.0 mm diameter aperture.

Ion Beam Formation (Momentum Analyzer and FS1, FS2, and FS3). The beam formation optics are similar to those used in the guided ion beam apparatus built by Armentrout and coworkers.[24] Ions emerging from the DFS are handled by focusing stage 1 (FS1), which is designed to shape and steer the beam and accelerate it to the voltage used for momentum analysis. In FS1, ions are extracted from the source and collimated by a double aperture immersion lens, focused by an einzel lens, and then accelerated to the momentum analysis potential. An electrostatic quadrupole doublet lens converts the beam from cylindrical symmetry to a ribbon shape appropriate for momentum analysis. The quadrupole doublets focus the beam onto the entrance slit of the momentum analyzer. A gate valve mounted on the flight tube of the analyzer (and biased at the mass analysis potential during operation) allows isolation of the source end of the instrument for changing source boats or for cleaning the source region without venting the entire instrument.

The magnetic momentum analyzer consists of a magnetic sector (Nuclide Corporation) with a 30.5 cm radius ion flight path and a 90° deflection angle. The entrance and exit slit widths are 1 mm. The analysis potential is typically 2800 V. Under these conditions, the momentum analyzer serves as a mass filter providing a mass range from 1 to 1500 Da, with a mass resolution of approximately 500 ($m/\Delta m$ fwhm) for ions with an initial energy spread of less than 1 eV.

After passing through the exit slit of the momentum analyzer, the ion beam is reconverted to cylindrical symmetry by a second electrostatic quadrupole doublet lens and focused by an einzel lens in FS2. A set of horizontal and vertical deflectors allows centering of the ion beam onto a 2 mm aperture, the entrance to the reaction vacuum chamber. This aperture also serves to separate vacuum regions for differential pumping. The ions enter an exponential retarder, which is 9.8 cm long and consists of 31 evenly spaced plates. The retarder plate potentials are determined by internally connected resistors that establish an exponentially decreasing field.[25] The last three plates are connected and their voltage controlled externally. These final plates act as the first lens in a four element lens sequence (FS3) that focuses and injects the ions into the octopole ion beam guide.

Interaction Region. The key part of the instrument is the interaction region, comprising an octopole ion beam guide surrounded by a gas reaction cell. The octopole radio frequency (rf) ion trap[26] provides a radial effective potential well for highly efficient collection of ionic reaction products. The octopole comprises eight rods of 3.2 mm diameter × 27.9 cm long, equally spaced on a bolt circle of 11.7 mm diameter. Opposing phases of the rf potential are applied to alternate rods. The rf is generated using a high voltage rf generator described by Jones et al.[27] The peak-to-peak amplitude of the rf potential is typically 300 V, which provides a trapping well of 2.83 V.[28] The dc bias of the octopole (and surrounding gas cell) is also controlled in order to vary the kinetic energy of the ions. This voltage is controlled by a Kepco BOP power supply under computer control.

Midway along its length, the octopole passes through a gas reaction cell. The gas cell consists of a 51 mm long × 51 mm diameter central body with smaller diameter extension tubes, 32 mm long × 17 mm diameter, extending from each end of the gas cell along the octopole rods, designed to limit gas conductance from the cell.[24] Two stainless steel tubes emanating perpendicularly from the gas reaction cell are electrically isolated from ground via glass to metal seals. These tubes are used to introduce the collision gas and measure pressure in the cell. A leak valve (Granville Phillips 203) is used to control the gas pressure introduced to the cell. The collision cell pressure is measured using a capacitance manometer (MKS Baratron 690A). Assuming a trapezoidal pressure profile,[24] the effective cell length is estimated to be 8.3 cm with a 10% uncertainty. Gas cell pressures in the range of 0.05 to 0.20 mTorr are generally used for cross section measurements, low enough that secondary reactions are minor contributors to the observed reactivity. In the present experiments, the collision gas is xenon, used for reasons described elsewhere.[22,29,30] During operation, a pressure difference ratio of approximately 70:1 can be maintained between the reaction cell and the main reaction vacuum chamber, which is continuously pumped by a 2000 L s^{-1} diffusion pump with water cooled baffles (Edwards Diffstak Mk2 250/2000P). To measure background signals arising from collisions that occur outside of the reaction cell, the gas flow can be diverted from the reaction cell directly to the main reaction vacuum chamber by switching remotely controlled electropneumatic valves on the gas inlet lines. In this configuration, the background pressure in the reaction chamber is the same as when the gas is flowing to the reaction cell. The effective length for background reactions is approximately twice as long as the reaction cell path length, resulting in a measured foreground/background ion intensity ratio of nearly 40:1.

Quadrupole Mass Spectrometer and Ion Detector. Ions drift to the end of the octopole ion guide, where they are extracted from the octopole and injected into the quadrupole mass spectrometer by a series of five lenses of cylindrical symmetry in focusing stage 4 (FS4). The quadrupole mass spectrometer (ABB Extrel) has a mass range up to 1000 Da, which is achieved with rods that are 19 mm in diameter, 22.9 cm long, and an oscillator frequency of 880 kHz. To achieve maximum transmission of ions, the quadrupole ordinarily is operated at a fairly low mass resolution.

Ions emanating from the quadrupole mass filter are then focused by a series of three lenses of cylindrical symmetry in the detector focusing stage. Ions are detected using a secondary electron scintillation detector of the Daly type,[31] operated at an ion target potential of 28 kV. This detector, combined with pulse counting electronics, provides high counting efficiency and low mass discrimination. The scintillation photons are detected using a photomultiplier tube (Burle model 8850). The output pulses of the photomultiplier are directly discriminated from noise using a constant fraction discriminator (Canberra model 2126) and counted using a dual counter timer (Canberra model 2071A) for digital data acquisition. A linear ratemeter (EG&G Ortec model 661) is used for visual display during tuning of the ion beam. The counting response of the ion detection system is linear up to $\sim 2 \times 10^7$ s^{-1}, and the counting noise background is less than 10 s^{-1}, providing a dynamic range in excess of 6 orders of magnitude.

Data Acquisition System. The guided ion beam apparatus is controlled by a personal computer equipped with a Pentium 133 MHz processor. Hardware control functions are provided by a commercial GPIB interface board (Keithley PCI-488) and a custom digital I/O board. The GPIB board has 12-bit resolution and controls a Canberra dual counter timer 2071A (used in ion detection) and a Kepco BOP 100−1M power supply (used to control the dc voltage applied to the reaction region). The BOP has two modes with high ($0 - \pm 100$ eV) and low ($0 - \pm 10$ eV) ranges, such that the 12-bit resolution of the GPIB results in a minimum energy step size of 0.002 eV below 10 and 0.024

eV above 10 eV. The digital I/O board contains a 16-bit optically isolated DAC used to set the mass for the quadrupole mass spectrometer. The minimum step size is 0.0153 Da. The digital I/O board also has two digital outputs connected to solid-state relays, which control electropneumatic valves that direct the neutral reactant gas to the reaction cell or reaction chamber. The I/O board also interfaces to the Baratron through a SCSI cable such that the pressure output is read digitally. All other ion lens potentials in the instrument and gas flow rates in the source and interaction regions need not vary with ion interaction energy and are therefore not automated. Lens potentials are provided by custom-built voltage dividers powered by standard dc power supplies. Gas flow rates are controlled manually with variable leak valves.

Two full 32-bit multithreaded graphical user interface (GUI) programs have been developed to control the instrument and acquire data during experiments. These programs are heavily modified and enhanced versions of the DOS-based predecessors originally developed by Armentrout and co-workers.[32] The programs are written using Compaq Visual Fortran Version 6.1A with lower level device interfaces written in C. The first program, MSCAN, allows the quadrupole mass spectrometer to be scanned at a fixed octopole interaction energy and records the intensity of detected ions as a function of mass. The second program, EMP (energy, mass, and pressure) allows the octopole interaction energy to be scanned and records the intensity of the specified reactant and product ions as a function of this energy. These programs have several features in common. Each program has real-time graphical display and I/O windows, a control panel, and a color and symbol palette. The control panel provides several functions: (1) it requires user input for instrument control and set up of a desired experiment, (2) in real time, it reports details and progress of the current experiment, and allows changes to be made in the graphical display window during data acquisition.

General Procedures. Ion intensities are converted to absolute cross sections as described previously.[24] Absolute uncertainties in cross section magnitudes are estimated to be ± 20%, which are largely the result of errors in the pressure measurement and the length of the interaction region. Relative uncertainties are approximately ± 5%. Because the radio frequency used for the octopole does not trap light masses with high efficiency, the cross sections for Li^+ products were more scattered and showed more variations in magnitude than is typical for heavier ions. Therefore, absolute magnitudes of the cross sections for production of Li^+ are probably accurate to ± 50%.

Ion kinetic energies in the laboratory frame, E_{lab}, are converted to energies in the center of mass frame, E_{CM}, using the formula $E_{CM} = E_{lab}\, m/(m + M)$, where M and m are the masses of the ionic and neutral reactants, respectively. All energies reported below are in the CM frame unless otherwise noted. The absolute zero and distribution of the ion kinetic energies are determined using the octopole ion guide as a retarding potential analyzer as previously described.[24] The distribution of ion kinetic energies is nearly Gaussian with a fwhm typically between 0.2 and 0.4 eV (lab) for these experiments. The uncertainty in the absolute energy scale is ± 0.05 eV (lab).

Even when the pressure of the reactant neutral is low, it has previously been demonstrated that the effects of multiple collisions can significantly influence the shape of CID cross sections.[23] Because the presence and magnitude of these pressure effects is difficult to predict, we have performed pressure-dependent studies of all cross sections examined here. In the present systems, we observe small cross sections at low energies that have an obvious dependence upon pressure. We attribute this to multiple energizing collisions that lead to an enhanced probability of dissociation below threshold. Data free from pressure effects are obtained by extrapolating to zero reactant pressure, as described previously.[23] Thus, results reported below are due to single bimolecular encounters.

Thermochemical Analysis. The threshold regions of the reaction cross sections are modeled using eq 1

$$\sigma(E) = \sigma_0 \sum_i g_i (E + E_i - E_0)^n / E \qquad (1)$$

where σ_0 is an energy independent scaling factor, E is the relative translational energy of the reactants, E_0 is the threshold for reaction of the ground electronic and ro-vibrational state, and n is an adjustable parameter. The summation is over the ro-vibrational states of the reactant ions, i, where E_i is the excitation energy of each state and g_i is the population of those states ($\Sigma g_i = 1$). The populations of excited ro-vibrational levels are not negligible even at 298 K as a result of the many low-frequency modes present in these ions. The relative reactivity of all ro-vibrational states, as reflected by σ_0 and n, is assumed to be equivalent.

To obtain model structures, vibrational frequencies, and energetics for the neutral and metalated *x*-MePyr, ab initio theory calculations were performed using Gaussian 98.[33] Geometry optimizations were performed at the MP2(full)/6-31G* level. Vibrational analyses of the geometry-optimized structures were performed to determine the vibrational frequencies and rotational constants of the molecules. When used to model the data or to calculate thermal energy corrections, the MP2(full)/6-31G* vibrational frequencies are scaled by a factor of 0.9646.[34] The scaled vibrational frequencies thus obtained for the 9 systems studied are available as supplementary information and listed in Table S1, whereas Table S2 lists the rotational constants.

The Beyer−Swinehart algorithm[35] is used to evaluate the density of the ro-vibrational states, and the relative populations g_i are calculated by an appropriate Maxwell−Boltzmann distribution at the 298 K temperature appropriate for the reactants. The average vibrational energy at 298 K of the metal ion-bound *x*-MePyr is also given in Table S1. We have estimated the sensitivity of our analysis to the deviations from the true frequencies by scaling the calculated frequencies to encompass the range of average scaling factors needed to bring calculated frequencies into agreement with experimentally determined frequencies found by Pople et al.[36] Thus, the originally calculated vibrational frequencies were increased and decreased by 10%. The corresponding change in the average vibrational energy is taken to be an estimate of one standard deviation of the uncertainty in vibrational energy (Table S1) and is included in the uncertainties, also reported as one standard deviation, listed with the E_0 values.

We also consider the possibility that collisionally activated complex ions do not dissociate on the time scale of our experiment (about 10^{-4} s) by including statistical theories for unimolecular dissociation, specifically Rice−Ramsperger−Kassel−Marcus (RRKM) theory, into eq 1 as described in detail elsewhere.[3,19] This requires sets of ro-vibrational frequencies appropriate for the energized molecules and the transition states (TSs) leading to dissociation. The former sets are given in Tables S1 and S2, whereas we assume that the TSs are loose and product-like because the interaction between the metal ion and the *x*-MePyr ligand is largely electrostatic. In this case, the TS vibrations used are the frequencies corresponding to the products, which are also found in Table S1. The transitional

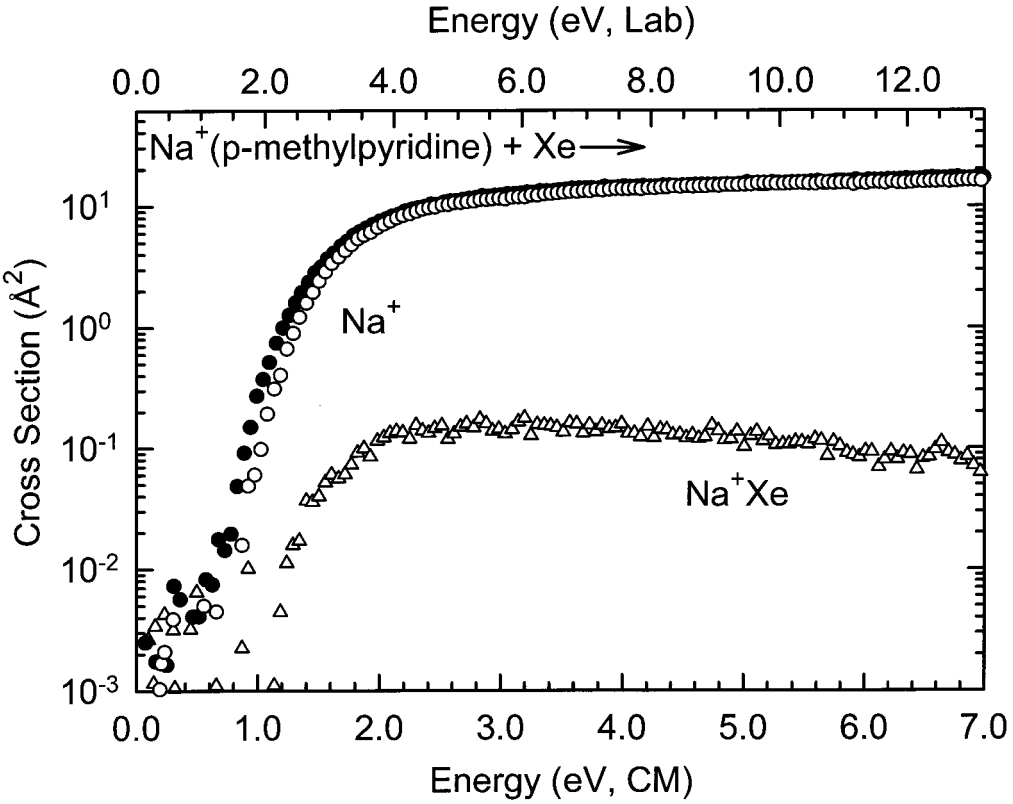

Figure 3. Cross sections for the collision-induced dissociation of the Na^+(*p*-methylpyridine) complex with Xe as a function of the center-of-mass frame collision energy (lower *x*-axis) and laboratory frame (upper *x*-axis). Data for the Na^+ product channel are shown for a Xe pressure of ~0.2 mTorr (●) and extrapolated to zero (○). The cross section for the ligand exchange process to form M^+Xe is also shown (△).

frequencies, those that become rotations of the completely dissociated products, are treated as rotors, a treatment that corresponds to a phase space limit (PSL) and is described in detail elsewhere.[3] For the M^+(*x*-MePyr) complexes, the two transitional mode rotors have rotational constants equal to those of the neutral *x*-MePyr product with axes perpendicular to the reaction coordinate. These are listed in Table S2. The external rotations of the energized molecule and TS are also included in the modeling of the CID data. The external rotational constants of the TS are determined by assuming that the TS occurs at the centrifugal barrier for interaction of M^+ with the neutral *x*-MePyr ligand, calculated variationally as outlined elsewhere.[3] The 2-D external rotations are treated adiabatically but with centrifugal effects included, consistent with the discussion of Waage and Rabinovitch.[37] In the present work, the adiabatic 2-D rotational energy is treated using a statistical distribution with explicit summation over the possible values of the rotational quantum number, as described in detail elsewhere.[3]

The model represented by eq 1 is expected to be appropriate for translationally driven reactions[38] and has been found to reproduce reaction cross sections well in a number of previous studies of both atom−diatom and polyatomic reactions,[39,40] including CID processes.[1,2,18,19,22,23,41−43] The model is convoluted with the kinetic energy distributions of both reactants, and a nonlinear least-squares analysis of the data is performed to give optimized values for the parameters σ_0, E_0, and n. The error associated with the measurement of E_0 is estimated from the range of threshold values determined for different data sets, variations associated with uncertainties in the vibrational frequencies, and the error in the absolute energy scale, 0.05 eV (lab). For analyses that include the RRKM lifetime effect, the uncertainties in the reported E_0 values also include the effects of increasing and decreasing the time assumed available for dissociation (10^{-4} s) by a factor of 2.

Equation 1 explicitly includes the internal energy of the ion, E_i. All energy available is treated statistically, which should be a reasonable assumption because the internal (rotational and vibrational) energy of the reactants is redistributed throughout the ion upon impact with the collision gas. The threshold for dissociation is by definition the minimum energy required leading to dissociation and thus corresponds to formation of products with no internal excitation. The assumption that products formed at threshold have an internal temperature of 0 K has been tested for several systems.[1,2,18,19,22,29] It has also been shown that treating all energy of the ion (vibrational, rotational, and translational) as capable of coupling into the dissociation coordinate leads to reasonable thermochemistry. The threshold energies for dissociation reactions determined by analysis with eq 1 are converted to 0 K bond energies by assuming that E_0 represents the energy difference between reactants and products at 0 K.[44] This assumption requires that there are no activation barriers in excess of the endothermicity of dissociation. This is generally true for ion−molecule reactions[39] and should be valid for the simple heterolytic bond fission reactions examined here.[45]

Results

Cross Sections for Collision-Induced Dissociation. Experimental cross sections were obtained for the interaction of Xe with nine M^+(*x*-MePyr) complexes, where $M^+ = Li^+$, Na^+, and K^+ and x = ortho, meta, and para. Figure 3 shows representative data for the Na^+(*p*-MePyr) complex. As discussed above, the dependence of the cross sections on pressure observed in the M^+ product data at the lowest energies, Figure 3, are a consequence of multiple collisions. A true single collision cross section for CID is obtained when the data are extrapolated to

TABLE 1: Threshold Dissociation Energies at 0 K and Entropies of Activation at 1000 K of M^+L[a]

M^+L	σ_0[b]	n[b]	E_0[c] (eV)	E_0(PSL) (eV)	kinetic shift (eV)	$\Delta S^\dagger$(PSL) (J mol^{-1} K^{-1})
Li^+(*o*-methylpyridine)	4.6 (0.6)	1.5 (0.1)	2.33 (0.11)	2.01 (0.07)	0.32	31 (2)
Na^+(*o*-methylpyridine)	23.0 (1.7)	1.2 (0.1)	1.38 (0.06)	1.33 (0.05)	0.05	35 (2)
K^+(*o*-methylpyridine)	27.0 (1.4)	0.9 (0.1)	1.03 (0.04)	1.01 (0.03)	0.02	32 (2)
Li^+(*m*-methylpyridine)	7.2 (2.9)	1.3 (0.2)	2.32 (0.21)	2.04 (0.14)	0.28	37 (2)
Na^+(*m*-methylpyridine)	21.4 (0.9)	1.1 (0.1)	1.45 (0.05)	1.38 (0.04)	0.07	32 (2)
K^+(*m*-methylpyridine)	20.8 (1.5)	0.9 (0.1)	1.05 (0.04)	1.03 (0.03)	0.02	24 (2)
Li^+(*p*-methylpyridine)	6.7 (3.3)	1.6 (0.2)	2.35 (0.19)	2.03 (0.14)	0.32	30 (2)
Na^+(*p*-methylpyridine)	21.9 (2.5)	1.0 (0.1)	1.47 (0.04)	1.39 (0.04)	0.08	25 (2)
K^+(*p*-methylpyridine)	33.9 (1.5)	0.9 (0.1)	1.03 (0.04)	1.02 (0.04)	0.01	17 (2)

[a] Uncertainties are listed in parentheses. [b] Average values for loose PSL transition state. [c] No RRKM analysis.

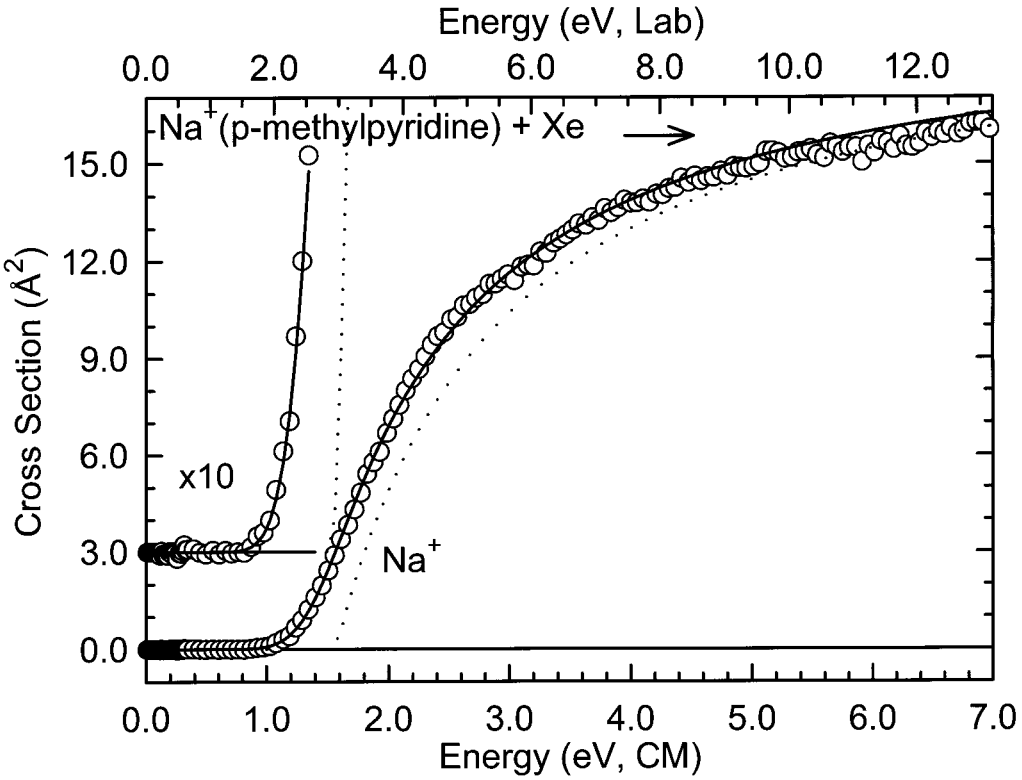

Figure 4. Zero pressure extrapolated cross section for collision-induced dissociation of the Na^+(*p*-methylpyridine) complex with Xe in the threshold region as a function of kinetic energy in the center-of-mass frame (lower *x*-axis) and the laboratory frame (upper *x*-axis). A solid line shows the best fit to the data using eq 1 convoluted over the neutral and ion kinetic energy distributions. A dashed line shows the model cross sections in the absence of experimental kinetic energy broadening for reactants with an internal energy corresponding to 0 K.

zero pressure of the Xe reactant as shown in Figure 3. The other M^+(*x*-MePyr) complexes show similar relative behavior. The most favorable process for all complexes is the loss of the intact *x*-MePyr molecule in the CID reactions 2.

$$M^+(x\text{-Mepyr}) + Xe \rightarrow M^+ + x\text{-Mepyr} + Xe \qquad (2)$$

The magnitudes of the cross sections increase in size from $M^+ = Li^+$ to Na^+ to K^+. This is largely because the thresholds decrease in this same order. The only other product that is observed in the CID reactions is the result of a ligand exchange process to form MXe^+. The cross sections for the MXe^+ products are approximately one to 3 orders of magnitude smaller than those of the primary dissociation product, M^+, and the thresholds are slightly lower (by the M^+-Xe binding energy), which is difficult to discern on the logarithmic scale. As little systematic information can be gleaned from these products, they will not be discussed further. However, it is conceivable that this ligand exchange process might cause a competitive shift in the observed thresholds. Within the quoted experimental errors, we do not believe such competition is likely to affect our threshold measurements in any of these systems for several reasons that have been detailed elsewhere.[46]

Threshold Analysis. The model of eq 1 was used to analyze the thresholds for reactions 2 in nine M^+(*x*-MePyr) systems. The results of these analyses are provided in Table 1 for all nine complexes and a representative analysis is shown in Figure 4 for the Na^+(*p*-MePyr) complex. In all cases, the experimental cross sections for reaction 2 are accurately reproduced using a loose PSL TS model.[3] Previous work has shown that this model provides the most accurate assessment of the kinetic shifts for CID processes for electrostatic ion−molecule complexes.[1−4,41,42] Good reproduction of the data is obtained over energy ranges exceeding 2.5 eV and cross section magnitudes of at least a factor of 100. Table 1 also includes values of E_0 obtained without including the RRKM lifetime analysis. Comparison of these values with the E_0(PSL) values shows that the kinetic shifts observed for these systems vary from 0.02 ± 0.01 eV for the K^+ systems, to 0.07 ± 0.02 eV for Na^+, and 0.31 ± 0.02 eV for Li^+. The total number of vibrations, 39, and heavy atoms, 8, remains the same in all of these M^+(*x*-MePyr) complexes and hence the number of low frequency vibrations remains the

TABLE 2: Enthalpies and Free Energies of Metal Ion Binding to Methylpyridines at 298 K in KJ/Mol[a]

system	ΔH_0	ΔH_0[b]	ΔH_{298}-ΔH_0[b]	ΔH_{298}	ΔH_{298}[b]	$T\Delta S_{298}$[b]	ΔG_{298}	ΔG_{298}[b]
H^+(*o*-methylpyridine)		925.7	5.8 (0.5)		931.5 (0.5)	23.3 (0.5)		908.2 (0.5)
Li^+(*o*-methylpyridine)	194.3 (6.5)	185.3	1.9 (1.6)	196.2 (6.7)	187.2 (1.6)	27.8 (3.5)	168.4 (7.6)	159.4 (3.8)
Na^+(*o*-methylpyridine)	128.2 (4.5)	129.3	1.0 (1.4)	129.2 (4.7)	130.3 (1.4)	29.5 (4.3)	99.7 (6.4)	100.8 (4.5)
K^+(*o*-methylpyridine)	97.8 (3.3)	93.8	0.7 (1.3)	98.5 (3.5)	94.5 (1.3)	28.9 (4.4)	69.6 (5.7)	65.6 (4.6)
H^+(*m*-methylpyridine)		923.3	6.1 (0.5)		929.4 (0.5)	27.7 (0.5)		901.7 (0.5)
Li^+(*m*-methylpyridine)	196.6 (14.7)	187.3	2.1 (1.7)	198.7 (14.8)	189.4 (1.6)	29.6 (3.4)	169.1 (15.2)	159.8 (3.8)
Na^+(*m*-methylpyridine)	133.3 (4.2)	130.6	0.9 (1.4)	134.2 (4.4)	131.5 (1.4)	29.2 (4.4)	105.0 (6.2)	102.3 (4.6)
K^+(*m*-methylpyridine)	99.8 (3.3)	96.7	0.3 (1.3)	100.1 (3.5)	97.0 (1.3)	27.6 (4.5)	72.5 (5.7)	69.4 (4.7)
H^+(*p*-methylpyridine)		925.5	5.9 (0.5)		931.4 (0.5)	26.0 (0.5)		905.4 (0.5)
Li^+(*p*-methylpyridine)	196.2 (13.4)	188.9	2.0 (1.6)	198.2 (13.5)	190.9 (1.6)	27.9 (3.5)	170.3 (13.9)	163.0 (3.8)
Na^+(*p*-methylpyridine)	133.7 (3.8)	132.0	0.7 (1.3)	134.4 (4.0)	132.7 (1.3)	27.5 (4.4)	106.9 (6.0)	105.2 (4.6)
K^+(*p*-methylpyridine)	98.8 (3.9)	97.7	0.2 (1.0)	99.0 (4.0)	97.9 (1.0)	26.0 (4.5)	73.0 (6.0)	71.9 (4.6)

[a] Uncertainties are listed in parentheses. [b] Ab initio values from calculations at the MP2(full)/6-311+G(2d,2p)//MP2(full)/6-31G* level of theory with frequencies scaled by 0.9646.

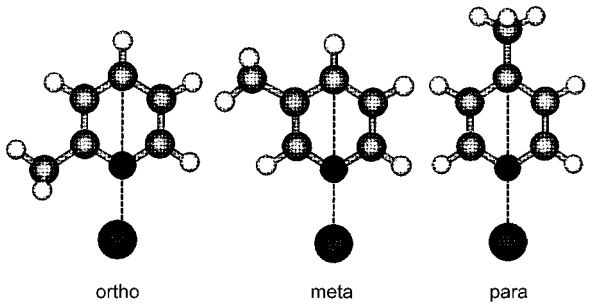

Figure 5. Optimized MP2(full)/6-31G* geometries of Na^+(*x*-methylpyridine), where x = ortho, meta, and para.

same. This implies that the observed kinetic shift should directly correlate with the density of states of the complex at threshold, which depends on the measured BDE. This is exactly what is found, as shown in Table 1.

The entropy of activation, $\Delta S^\dagger$, is a measure of the looseness of the TS and also a reflection of the complexity of the system. It is largely determined by the molecular parameters used to model the energized molecule and the TS, but also depends on the threshold energy. Listed in Table 1, $\Delta S^\dagger$(PSL) values at 1000 K show modest variation, as expected on the basis of the similarity of these systems, and range between 17 and 37 J mol^{-1} K^{-1} across these systems. These entropies of activation can be favorably compared to $\Delta S^\dagger_{1000}$ values in the range of 29 to 46 J K^{-1} mol^{-1} collected by Lifshitz for several simple bond cleavage dissociations of ions.[47]

Theoretical Results. Theoretical structures for neutral *x*-MePyr ligands and for the complexes of these ligands with H^+, Li^+, Na^+, and K^+ were calculated as described above. Table S3 gives details of the final geometries for each of these species. The results for the most stable conformation of each Na^+(*x*-MePyr) complex are shown in Figure 5.[48]

Not surprisingly, the calculations find that the metal ions and proton prefer to be bound to the nitrogen atom in the plane of *x*-MePyr rather than to the π-cloud of the aromatic ring. In general, the distortion of the *x*-MePyr molecule that occurs upon complexation to a metal ion or proton is minor. The change in geometry is largest for the protonated systems and decreases with increasing size of the cation. Bond lengths and angles change in the most extreme cases by less than 0.01 Å and 8.1°, respectively. An interesting result is observed in the ortho complexes in that the metal ion is displaced slightly toward the methyl group, see Figure 5. The displacement is metal ion dependent with a ∠C4−N−M angle of 175.9°, 176.4°, and 179.2° for the ortho complexes to Li^+, Na^+, and K^+, respectively. In contrast, the meta and para complexes to all of the metals have ∠C4−N−M bond angles that are within 0.2° of linear.

Conversion from 0 to 298 K. To allow comparison to previous literature values[12−14,49] and commonly used experimental conditions, we convert the 0 K bond energies determined here experimentally and theoretically to 298 K bond enthalpies and free energies. The enthalpy and entropy conversions are calculated using standard formulas (assuming harmonic oscillator and rigid rotor models) and the vibrational and rotational constants determined for the MP2(full)/6-31G* optimized geometries, which are given in Tables S1 and S2. Table 2 lists 0 and 298 K enthalpy, free energy, and enthalpic and entropic corrections for all systems experimentally determined (from Table 1). Uncertainties in the enthalpic and entropic corrections are determined by 10% variation in the molecular constants. For the metal systems where the metal−ligand frequencies are very low and may not be adequately described by theory, the listed uncertainties also include changing the three metal−ligand frequencies by a factor of 2. The latter provides a conservative estimate of the computational errors in these low-frequency modes and is the dominant source of the uncertainties listed.

In addition, we have adjusted the free energy value for Li+(*m*-MePyr) of 152.7 ± 8.0 kJ/mol taken from the work of Taft and co-workers (listed at 373 K) to 0 K.[12−14] The uncertainty in this value is the uncertainty of the anchor used, $Li^+(H_2O)$ taken from work of Rodgers and Armentrout.[4] The conversion values required here are $T\Delta S_{373}$ = 37.6 ± 4.7 kJ/mol and that $\Delta H_{373} - \Delta H_0$ = 2.0 ± 1.9 kJ/mol. The resultant value of 188.3 ± 9.5 kJ/mol is compared to the present results in Table 3 and Figure 6 and discussed further below.

Discussion

Comparison of Theory and Experiment. The metal cation affinities of the three structural isomers of *x*-MePyr at 0 K measured here by guided ion beam mass spectrometry are summarized in Table 3. Also listed here are the 0 K proton and metal binding energies calculated at the MP2(full)/6-311+G(2d,2p)//MP2(full)/6-31G* level including full MP2 correlation, zero point energy corrections, and basis set superposition error corrections.[50−52] Previous theoretical results for the unsubstituted pyridine molecule taken from previous studies are also provided in Table 3 for comparison. The agreement between theory and experiment is illustrated in Figure 6. It can be seen that the agreement is very good over the nearly 100 kJ/mol variation in binding affinities measure here. For the nine methyl-substituted systems, the mean absolute deviation (MAD) between experiment and theory is 4.4 ± 3.3 kJ/mol. This is slightly smaller than the average experimental error of 6.4 ±

TABLE 3: Calculated Enthalpies of Proton and Alkali Metal Ion Binding to Methyl Pyridines at 0 K in KJ/Mol

	experiment		theory (MP2)		
complex	TCID[a]	literature	D_e[b]	D_0[c]	$D_{0,BSSE}$[d]
H^+(*o*-methylpyridine)		943.3	971.6	935.4	925.7
Li^+(*o*-methylpyridine)	194.3 (6.5)		197.1	191.5	185.3
Na^+(*o*-methylpyridine)	128.2 (4.5)		139.1	135.4	129.3
K^+(*o*-methylpyridine)	97.8 (3.3)		101.2	98.0	93.8
H^+(*m*-methylpyridine)		937.3 (16.0)[e]	968.9	932.7	923.3
		905.6(16.0)[e]			
Li^+(*m*-methylpyridine)	196.6 (14.7)	188.3 (9.5)[f]	198.8	192.9	187.3
Na^+(*m*-methylpyridine)	133.3 (4.2)		140.5	137.0	130.6
K^+(*m*-methylpyridine)	99.8 (3.3)		103.0	100.5	96.7
H^+(*p*-methylpyridine)		941.3 (16.0)[e]	970.7	934.9	925.5
Li^+(*p*-methylpyridine)	196.2 (13.4)		200.2	194.5	188.9
Na^+(*p*-methylpyridine)	133.7 (3.8)		141.6	138.3	132.0
K^+(*p*-methylpyridine)	98.8 (3.9)		104.0	101.3	97.7
H^+(pyridine)		924.0 (16.0)[e]	954.8[g]	918.4[g]	908.9[g]
Li^+(pyridine)	181.0 (14.5)[g]	181.2 (9.5)[f]	190.7[g]	185.7[g]	179.1[g]
Na^+(pyridine)	126.7 (2.9)[g]		133.6[g]	130.1[g]	122.9[g]
K^+(pyridine)	90.3 (3.9)[g]		97.2[g]	94.6[g]	91.1[g]

[a] Present results, threshold collision-induced dissociation. [b] Calculated at the MP2(full)/6-311+G(2d,2p) level of theory using MP2(full)/6-31G* optimized geometries. [c] Including zero point energy corrections with frequencies scaled by 0.9646. [d] Also includes basis set superposition error corrections. [e] Ref 50. Adjusted to 0 K. [f] Ref 12−14. Adjusted to 0 K as described in the text. [g] Ref 8.

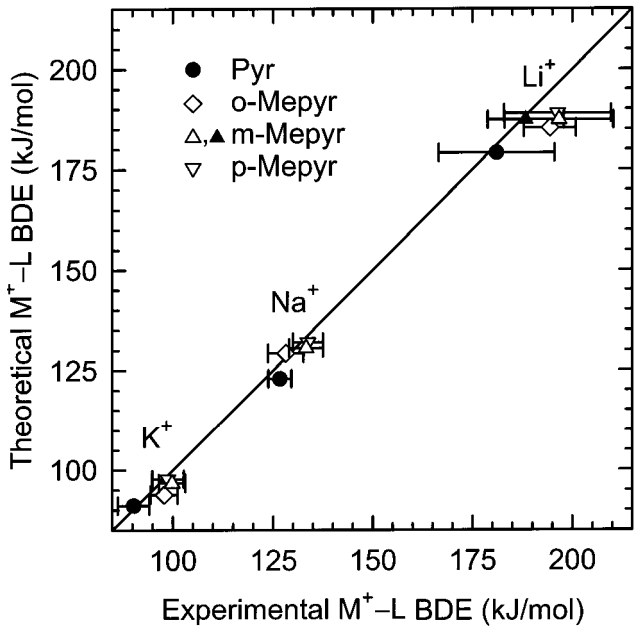

Figure 6. Experimental bond dissociation energies (in kJ/mol) of M^+−(*x*-methylpyridine), where $M^+ = Li^+$, Na^+, and K^+, and x = ortho (◇), meta (△), and para (▽). Experimental results include values from ref 8 (●) and ref 12−14 (▲). All values are at 0 K.

4.5 kJ/mol. However, more careful inspection of the data makes it clear that Li+ is the principal contributor to the deviations. For the three Li^+ systems, the MAD is 8.5 ± 1.1 kJ/mol, whereas the Na^+ and K^+ systems have a MAD of 2.3 ± 1.2 kJ/mol. The poorer agreement for the Li^+ systems may result from the experimental difficulty in measuring cross sections for Li^+ as a result of the difficulty associated with efficient detection of this light mass as discussed in the Experimental Section. An alternative explanation was proposed in an earlier study[9] where it was also observed that theory systematically underestimates the bond energies for the Li^+ complexes, which may be a result of the higher degree of covalency in the metal−ligand bond (see discussion below). The additional covalency of the metal−ligand bonds in the Li^+ systems compared to those for Na^+ and K^+ suggests that this level of theory may be inadequate for a complete description of the former systems. Some evidence for this is the even larger discrepancy between theoretical and experimental values for the protonated systems, Table 3, which are clearly covalent. However, it is also possible that this additional covalency means that the transition states for dissociation of the Li^+ complexes are not adequately described by the PSL model. If the transition states were tighter in the Li^+ cases, then the kinetic shifts would be larger and the thresholds measured smaller, in better agreement with theory. For the Na^+ and K^+ complexes, the kinetic shifts are much smaller and the metal−ligand bonds less electrostatic, such that the treatment here is probably appropriate and would not change greatly with different assumptions about the transition state.

Comparison with Literature Values. Table 3 and Figure 6 also compare the present experimental results to those of Taft and co-workers on Li^+(*m*-MePyr).[12−14] Using ion cyclotron resonance (ICR) mass spectrometry, Anvia et al.[12] measured the Gibbs free energy for Li^+ binding to *m*-MePyr relative to pyridine, finding a difference of 6.3 kJ/mol in favor of the substituted pyridine. Taft et al.[13] placed these values (and many others) on an absolute scale by using results of Woodin and Beauchamp,[53] who in turn referenced their values to that for $Li^+(H_2O)$ taken from Dzidic and Kebarle.[54] Recently, Rodgers and Armentrout[2] have noted that the anchoring process used by Taft et al.[13] was flawed, a conclusion that has been substantiated by work of Burk et al.[14] In this latter work, the early results of Taft et al. have been revised and placed on an absolute scale using the bond energy for $Li^+(H_2O)$ taken from Rodgers and Armentrout.[1] This agrees well with a revised value published subsequently[4] but with a smaller uncertainty of 8.0 kJ/mol. We assign this latter value as the absolute uncertainty of the lithium cation basicity scale given by Burk et al. and then adjust their value for Li^+(*m*-MePyr) to 0 K as discussed above. The resulting value is in good agreement with theory and the value measured here.

Trends in the Binding of Metal Ions to *x*-Methylpyridines. In all of the *x*-MePyr systems, the binding strength varies with the metal ion such that Li^+ binds ∼35% more strongly than Na^+, which in turn binds ∼50% more strongly than K^+. As these complexes are largely electrostatic in nature, this trend is a consequence of the varying size or equivalently the charge density of the metal ion. Smaller metal ions lead to stronger ion−dipole and ion-induced dipole interactions in these systems because the metal−ligand bond distances are smaller. Calcula-

tions indicate that the charge retained on the metal follows the order Li^+ ($\sim$0.72*e*) < Na^+ ($\sim$0.91*e*) < K^+ ($\sim$0.98*e*). The shorter bond distance and greater charge density in the smaller cations allows the metal ion to more effectively withdraw electron density from the neutral ligand, thus reducing the charge retained on the metal and increasing the covalency of the metal−ligand interaction.

The primary effect that the methyl substituent has upon the binding can be examined by comparing these systems to the unsubstituted pyridine molecule. The polarizability of pyridine is estimated to be 9.51 Å^3 and increases to 11.35 Å^3 upon methyl substitution.[11] The polarizability is not expected to vary significantly with the position of the methyl substituent, and the additivity method we used to estimate these polarizabilities is not sensitive to such structural differences. The binding affinity of all nine complexes is observed to increase upon methyl substitution relative to that observed for the corresponding pyridine complexes, Table 3 and Figure 6. This suggests that the polarizability of the ligand is a key factor in determining the strength of binding.

Much smaller variations in the strength of the binding are observed as the position of the substituent is varied. These variations can be attributed to several possible effects; the dipole moment of the molecule, resonance or inductive effects, and steric effects. As seen in Figure 1, the dipole moment of these systems follows the order ortho < meta < para. The calculated dipole moment of pyridine is 2.22 D, implying that if the dipole moment plays an important role in determining the binding strength, that the ortho substituted complexes should have lower binding affinities than pyridine. This is not the case in Table 3, suggesting that the polarizability is more important than the dipole moment of the ligand in determining the strength of binding as mentioned above. The dipole moment may still play a role, albeit less significant, and suggests that the binding affinities should follow the order ortho < meta < para. Because of the electron donating properties of the methyl substituent, resonance or inductive effects suggest that the binding affinities should follow the order meta < ortho $\approx$ para. (Indeed, this is the order observed in the protonated complexes, where the longer-range electrostatic interactions are not expected to play as strong a role as for the metalated systems.) Steric repulsion between the methyl substituent and the metal ion would suggest that the binding affinities should follow the order ortho < meta $\approx$ para, but a chelation interaction with the adjacent methyl group would predict a meta $\approx$ para < ortho order. Both theory and experiment find that the ortho substituted complexes are the most weakly bound for all three metal ions, Table 3. This suggests that either the dipole moment of the ligand or steric effects are more important than inductive effects. In all three ortho substituted complexes, the metal ion orients itself such that it is actually slightly tilted toward the methyl substituent (by 4.1°, 3.6°, and 0.8° for the Li^+, Na^+ and K^+ systems, respectively), Figure 5. This suggests there is chelation (attractive interaction) with the adjacent methyl group rather than a steric effect (repulsive interaction), but that steric interactions between the metal ion and the substituent increase with the size of the metal ion as might be expected. Especially considering the structural evidence for chelation, the weaker binding observed for the ortho complexes can thus be attributed to the smaller dipole moment of this molecule. The case is not quite so clear-cut for the meta and para systems. Theory finds that the meta systems bind more weakly than the para systems, in agreement with the expected order based upon the dipole moments of these molecules and inductive effects. But, it has already been established in the ortho systems that the dipole moment has a greater influence on the binding than inductive effects of the substituent. Therefore, the observed relative order is likely the result of the dipole moment of these ligands. In contrast, the measured binding affinities for the meta and para systems are essentially equal. This suggests that the influence of the dipole moment and inductive effects on the binding to these systems are quite small. Overall, the observed trends in the binding of alkali metal ions to these systems are therefore dominated by the charge density of the metal ion and secondarily by the polarizability of the ligand. The dipole moment of the ligand, inductive effects, chelation, and steric interactions appear to influence the binding in these systems very little.

Conclusions

The kinetic energy dependences of the collision-induced dissociations of M^+(*x*-MePyr), where $M^+ = Li^+$, Na^+, and K^+, and *x* = ortho, meta, and para with Xe are examined in a guided ion beam mass spectrometer. The dominant dissociation process in all cases is loss of the intact *x*-MePyr ligand. Thresholds for these processes are determined after consideration of the effects of reactant internal energy, multiple collisions with Xe, and lifetime effects (using methodology described in detail elsewhere).[3] Insight into the structures and binding of the metal ions to the *x*-MePyr molecules is provided by ab initio theory calculations of these complexes performed at the MP2(full)/6-311+G(2d,2p)//MP2(full)/6-31G* level of theory. Excellent agreement between the experimentally determined Na^+ and K^+ affinities and ab initio calculations is obtained. However, within experimental error, the agreement for the Li^+ systems is not quite as good. Several plausible explanations for this discrepancy are proposed. Good agreement is also found for the single previously measured BDE for Li^+−*m*-Mepyr determined by ion−molecule reaction equilibrium measurements in a FT-ICR spectrometer.[12−14] The high fidelity of our experimental and theoretical results and the single previously measured value suggests that these ligands can act as reliable anchors for the alkali metal cation affinity scales. These systems broaden the range of ligands available as absolute thermochemical anchors. Further, the combined theoretical and experimental results suggest that the charge density of the metal ion and the polarizability of the ligand are the dominant factors that determine the strength of these noncovalent interactions. The dipole moment of the ligand, inductive effects, and steric interactions appear to influence the binding in these systems very little.

Acknowledgment. This work was supported in part by an ASMS Research Award from Micromass.

Supporting Information Available: Vibrational frequencies and vibrational energies at 298 K (Table S1), rotational constants (Table S2), MP2(full)/6-31G* geometry optimized structures (Table S3), cross sections (Fig S1), and zero pressure extrapolated cross sections (Fig S2) of the methylpyridines discussed in the text. This material is available free of charge via the Internet at http://pubs.acs.org.

Note Added after ASAP Posting: This manuscript was originally posted to the web on 02/14/01 without reference to the Supporting Information. The corrected version was posted on 3/15/01.

References and Notes

(1) Rodgers, M. T.; Armentrout, P. B. *J. Phys. Chem. A* **1997**, *101*, 1238.

(2) Rodgers, M. T.; Armentrout, P. B. *J. Phys. Chem. A* **1997**, *101*, 2614.
(3) Rodgers, M. T.; Ervin, K. M.; Armentrout, P. B. *J. Chem. Phys*. **1997**, *106*, 4499.
(4) Rodgers, M. T.; Armentrout, P. B. *J. Chem. Phys*. **1998**, *109*, 1787.
(5) Rodgers, M. T.; Armentrout, P. B. *Int. J. Mass Spectrom*. **1999**, *185/186/187*, 359.
(6) Rodgers, M. T.; Armentrout, P. B. *J. Phys. Chem. A* **1999**, *103*, 4955.
(7) Armentrout, P. B.; Rodgers, M. T. *J. Phys. Chem. A* **2000**, *104*, 2238.
(8) Amunugama, R.; Rodgers, M. T. *Int. J. Mass Spectrom*. **2000**, *195/196*, 439.
(9) Rodgers, M. T.; Armentrout, P. B. *J. Am. Chem. Soc*. **2000**, *122*, 8548.
(10) Rodgers, M. T.; Stanley, J. R.; Amunugama, R. *J. Am. Chem. Soc*. **2000**, *122*, 10 969.
(11) Miller, K. J. *J. Am. Chem. Soc*. **1990**, *112*, 8533.
(12) Anvia, F.; Walsh, S.; Capon, M.; Koppel, I. A.; Taft, R. W.; de Paz, J. L. G.; Catalan, J. *J. Am. Chem. Soc.* **1990**, *112*, 5095.
(13) Taft, R. W.; Anvia, F.; Gal, J.-F.; Walsh, S.; Capon, M.; Holmes, M. C.; Hosn, K.; Oloumi, G.; Vasanwala, R.; Yazdani, S. *Pure Appl. Chem.* **1990**, *62*, 17.
(14) Burk, P.; Koppel, I. A.; Koppel, I.; Kurg, R.; Gal, J.-F.; Maria, P.-C.; Herreros, M.; Notario, R.; Abboud, J.-L. M.; Anvia, F.; Taft, R. W. *J. Phys. Chem. A* **2000**, *104*, 2824.
(15) Schultz, R. H.; Armentrout, P. B. *Int. J. Mass Spectrom. Ion Processes* **1991**, *107*, 29.
(16) Graul, S. T.; Squires, R. R. *Mass Spectrom. Rev*. **1988**, *7*, 263.
(17) Ferguson, E. E.; Fehsenfeld, F. C.; Schmeltekopf, A. L. *Adv. At. Mol. Phys.* **1969**, *5*, 1.
(18) Schultz, R. H.; Crellin, K. C.; Armentrout, P. B. *J. Am. Chem. Soc.* **1991**, *113*, 8590.
(19) Khan, F. A.; Clemmer, D. C.; Schultz, R. H.; Armentrout, P. B. *J. Phys. Chem*. **1993**, *97*, 7978.
(20) Schultz, R. H.; Armentrout, P. B. *J. Chem. Phys*. **1992**, *96*, 1046.
(21) Fisher, E. R.; Kickel, B. L.; Armentrout, P. B. *J. Phys. Chem*. **1993**, *97*, 10 204.
(22) Dalleska, N. F.; Honma, K.; Armentrout, P. B. *J. Am. Chem. Soc.* **1993**, *115*, 12 125.
(23) Dalleska, N. F.; Honma, K.; Sunderlin, L. S.; Armentrout, P. B. *J. Am. Chem. Soc*. **1994**, *116*, 3519.
(24) Ervin, K. M.; Armentrout, P. B. *J. Chem. Phys*. **1985**, *83*, 166.
(25) Vestal, M. L.; Blakley, C. R.; Ryan, P. B.; Futrell, J. H. *Rev. Sci. Instrum*. **1976**, *47*, 15.
(26) Teloy, E.; Gerlich, D. *Chem. Phys.* **1974**, *4*, 417. Gerlich, D.; Diplomarbeit, University of Freiburg, Federal Republic of Germany, 1971. Gerlich, D. In *State-Selected and State-to-State Ion−Molecule Reaction Dynamics, Part I, Experiment*; Ng, C.-Y., Baer, M., Eds.; *Adv. Chem. Phys.* **1992**, *82*, 1.
(27) Jones, R. M.; Gerlich, D.; Anderson, S. L. *Rev. Sci. Instrum.* **1997**, *68*, 3357.
(28) Muntean; F.; Armentrout, P. B., work in progress.
(29) Aristov, N.; Armentrout, P. B. *J. Phys. Chem.* **1986**, *90*, 5135.
(30) Hales, D. A.; Armentrout, P. B. *J. Cluster Sci.* **1990**, *1*, 127.
(31) Daly, N. R.; *Rev. Sci. Instrum.* **1959**, *31*, 264.
(32) Armentrout, P. B., personal communication.
(33) Gaussian 98, Revision A.7, Frisch, M. J.; Trucks, G. W.; Schlegel, H. B.; Scuseria, G. E.; Robb, M. A.; Cheeseman, J. R.; Zakrzewski, V. G.; Montgomery Jr., J. A.; Stratmann, R. E.; Burant, J. C.; Dapprich, S.; Millam, J. M.; Daniels, A. D.; Kudin, K. N.; Strain, M. C.; Farkas, O.; Tomasi, J.; Barone, V.; Cossi, M.; Cammi, R.; Mennucci, B.; Pomelli, C.; Adamo, C.; Clifford, S.; Ochterski, J.; Petersson, G. A.; Ayala, P. Y.; Cui, Q.; Morokuma, K.; Malick, D. K.; Rabuck, A. D.; Raghavachari, K.; Foresman, J. B.; Cioslowski, J.; Ortiz, J. V.; Stefanov, B. B.; Liu, G.; Liashenko, A.; Piskorz, P.; Komaromi, I.; Gomperts, R.; Martin, R. L.; Fox, D. J.; Keith, T.; Al-Laham, M. A.; Peng, C. Y.; Nanayakkara, A.; Gonzalez, C. Challacombe, M.; Gill, P. M. W.; Johnson, B.; Chen, W. Wong, M. W.; Andres, J. L.; Gonzales, C.; Head-Gordon, M.; Replogle, E. S.; Pople, J. A. Gaussian, Inc. Pittsburgh, PA, 1998.
(34) Foresman, J. B.; Frisch, Æ. *Exploring Chemistry with Electronic Structure Methods*, 2nd Ed.; Gaussian: Pittsburgh, 1996.
(35) Beyer, T. S.; Swinehart, D. F. *Comm. Assoc. Comput. Machines* **1973**, *16*, 379. Stein, S. E.; Rabinovitch, B. S. *J. Chem. Phys*. **1973**, *58*, 2438; *Chem. Phys. Lett*. **1977**, *49*, 1883.
(36) Pople, J. A.; Schlegel, H. B.; Raghavachari, K.; DeFrees, D. J.; Binkley, J. F.; Frisch, M. J.; Whitesides, R. F.; Hout, R. F.; Hehre, W. J. *Int. J. Quantum Chem. Symp*. **1981**, *15* 269. DeFrees, D. J.; McLean, A. D. *J. Chem. Phys*. **1985**, *82*, 333.
(37) Waage, E. V.; Rabinovitch, B. S. *Chem. Rev*. **1970**, *70*, 377.
(38) Chesnavich, W. J.; Bowers, M. T. *J. Phys. Chem.* **1979**, *83*, 900.
(39) Armentrout, P. B.; In *Advances in Gas-Phase Ion Chemistry*; Adams, N. G.; Babcock, L. M., Eds.; JAI.; Greenwich, 1992; Vol. 1, pp 83−119.
(40) See, for example: Sunderlin, L. S.; Armentrout, P. B. *Int. J. Mass Spectrom. Ion Processes* **1989**, *94*, 149.
(41) More, M. B.; Glendening, E. D.; Ray, D.; Feller, D.; Armentrout, P. B. *J. Phys. Chem*. **1996**, *100*, 1605.
(42) Ray, D.; Feller, D.; More, M. B.; Glendening, E. D.; Armentrout, P. B. *J. Phys. Chem*. **1996**, *100*, 16 116.
(43) Meyer, F.; Khan, F. A.; Armentrout, P. B. *J. Am. Chem. Soc*. **1995**, *117*, 9740.
(44) See, for example: Figure 1 in ref 22.
(45) Armentrout, P. B.; Simons, J. *J. Am. Chem. Soc.* **1992**, *114*, 8627.
(46) Meyer, F.; Khan, F. A.; Armentrout, P. B. *J. Am. Chem. Soc*. **1995**, *117*, 9740.
(47) Lifshitz, C. *Adv. Mass Spectrom*. **1989**, *11*, 113.
(48) Figures were generated using the output of Gaussian98 geometry optimizations in Hyperchem Computational Chemistry Software Package, Version 5.0, Hypercube Inc., 1997.
(49) Hunter, E. P.; Lias, S. G. *Proton Affinity Evaluation in NIST Chemistry WebBook, NIST Standard Reference Database Number 69*; Mallard,W. G., Lindstrom, P. J., Eds.; National Institute of Standards and Technology, Gaithersburg MD, 1998, (http://webbook.nist.gov).
(50) Møller, C.; Plesset, M. S. *Phys. Rev*. **1934**, *46*, 618.
(51) Bartlett, R. J. *Annu. Rev. Phys. Chem.* **1981**, *32*, 359.
(52) Hehre, W. J.; Radom, L.; Schleyer, P. v. R.; Pople, J. A. *Ab Initio Molecular Orbital Theory*; Wiley: New York, 1986.
(53) Woodin, R. L.; Beauchamp, J. L. *J. Am. Chem. Soc*. **1978**, *100*, 501.
(54) Dzidic, I.; Kebarle, P. *J. Phys. Chem.* **1974**, *74*, 1466.